Utilizing an Improved EXAFS Structure Analysis Method to Reveal Site-Specific Bonding Properties of $Ag_{44}(SR)_{30}$ Nanoclusters

Ziyi Chen[†], *Daniel M. Chevrier*[†,1], *Brian E. Conn*[‡2], *Terry P. Bigioni*[‡], *Peng Zhang*[*,†]

[†] Department of Chemistry, Dalhousie University, Halifax, Nova Scotia, B3H 4R2, Canada

[‡] Department of Chemistry and Biochemistry, University of Toledo, Toledo, Ohio 43606, United States

[1] Current address is Aix-Marseille University, French Alternative Energies and Atomic Energy Commission (CEA), French National Center for Scientific Research (CNRS), UMR7265 Institute of Biosciences and Biotechnologies of Aix-Marseille (BIAM), Saint-Paul-lez-Durance, 13108 France

2 Current address is Adhesive Technologies and Functional Coatings, Henkel Corporation, Madison Heights, MI 48071, United States

KEYWORDS

silver nanoclusters, $Ag_{44}(SR)_{30}$, extended X-ray absorption fine structure (EXAFS), bonding properties, fitting method

ABSTRACT

Atomically precise nanoclusters (NCs) are of great interest due to their well-defined structures and molecule-like properties. Understanding their structure-property relationship is an important task because it can help tailor their structures to achieve specific desired properties. In this study, the temperature-dependent bonding properties of $Ag_{44}(SR)_{30}$ have been revealed by the extended X-ray absorption fine structure (EXAFS) with a new structure analysis method, which includes two Ag-S and two Ag-Ag fitting shells. It has been proven that the EXAFS fitting quality can be improved significantly compared with the conventional method. New insights into Ag-S bondings were discovered based on the fitting results obtained from the new method. It allows us to observe two different bonding properties within the Ag-S motifs, which cannot be discovered by using the conventional method. Additionally, the metal core of $Ag_{44}(SR)_{30}$ exhibits uncommon thermal behavior, which could be connected to the absence of the center atom in the icosahedral core. Our results demonstrate that the new structure analysis method can provide a more reliable comparison of NCs structural changes than the conventional method and it could be applicable to other NCs. The revealed temperature-dependent bonding properties can provide insights into the structure-property relationship of $Ag_{44}(SR)_{30}$, which can help design new NCs materials with tailored properties.

1. INTRODUCTION

Atomically precise nanoclusters (NCs) have been studied for many years due to their unique physical and chemical properties.[1–4] Such NCs normally have particle diameters less than 3 nm, and have a molecular structure, i.e. an exact number and arrangement of atoms in each NCs. In recent years, more and more thiolate-protected NCs have been synthesized and their structures were determined by single crystal X-ray diffraction.[5–9] Many of them possess structures that are not commonly observed in traditional nanoparticles.[10–12] Understanding their properties therefore becomes critical for developing a better understanding of the structure-property relationships and thereby determine their potential applications. Among the great variety of thiolate-protected NCs, Ag NCs and Au NCs are two major groups in this field. However, the study of Ag NCs is less well-developed than Au NCs because of the lower stability of Ag NCs. In 2013, Na_4Ag_{44}(*p*-mercaptobenzoic acid)$_{30}$ ($Ag_{44}(SR)_{30}$ for short) was shown to have such high stability that it could be synthesized in quantitative yields and on a large scale.[6] The study of structure and bonding properties under different conditions would be useful since it could provide a deeper understanding of the stability of such materials.

X-ray absorption spectroscopy (XAS) is a powerful technique to study both electronic properties and bonding properties within one spectrum.[13] The X-ray absorption near edge structure (XANES) has been successfully applied to investigate the electronic properties of NCs.[14–17] The extended X-ray absorption fine structure (EXAFS) is the region of XAS about 50 eV above the edge, which is useful for investigating the element-specific local structural environment of thiolate protected NCs under different conditions.[18–22] It has already been applied to study temperature effect on 25-atom NCs.[20,21] Generally, a thiolate protected NC has several different coordination environments, and the bond distances can be grouped into distinct shells. One major

advantage of EXAFS is that it allows the observation of bond distance changes for each shell. Thus, the determination of fitting shells is a critical step. Simulated wavelet-transformed EXAFS (WT-EXAFS) has been successfully applied to determine the fitting shells of EXAFS for Ag_{25} NCs.[21] The WT-EXAFS have both information from distance (FT-EXAFS) and energy perspective (*k* space). When two types of bonds have similar bond distances, they can merge into one peak in FT-EXAFS, which can be resolved based on the wavenumber of *k* space in WT-EXAFS.[23–25] Most of the previous EXAFS studies on thiolate protected NCs focused on distinguishing the metal-metal (M-M) shells.[19,20,22,26,27] In this study, we present a Ag K-edge EXAFS analysis on solid phase $Ag_{44}(SR)_{30}$ at 90 K and 300 K by using a new structure analysis method where two Ag-ligand shells were applied. The simulated WT-EXAFS method was utilized to determine the fitting shells. Then, the detailed structural changes on Ag-ligand shells and M-M shells of $Ag_{44}(SR)_{30}$ were uncovered from the fitting results of the improved fitting method.

2. METHODOLOGY

2.1 Synthesis of NCs

The detailed synthesis procedure of $Ag_{44}(SR)_{30}$ NCs has been published previously.[6,28] Briefly, the Ag-thiolate precursor was synthesized by combining aqueous $AgNO_3$ with ethanolic *p*-mercaptobenzoic acid (*p*-MBA). Aqueous $NaBH_4$ was used to reduce the precursor to form the $Ag_{44}(SR)_{30}$ NCs. The NCs were isolated by precipitation with dimethylformamide (DMF).

2.2 XAS Measurements and Fitting Method

The Ag K-edge XAS spectra were collected at the Sector 20-BM beamline at the Advanced Photon Source (operating at 7.0 GeV). For data collected at 90 K, a helium-cooled cryostat

chamber was used for measurement. The detailed description of the sample preparation for XAS measurement has been reported previously.[18] The fitting of EXAFS spectra were performed by Artemis and Athena.[29] The amplitude reduction factor (S_0^2) was fixed at 0.90, which was determined from a Ag foil reference. The k_2-weighting was applied for all fittings. A k-range of 3-12 $Å^{-1}$ was used for data collected at 90 K and the four-shell fitting of data collected at 300 K. A shorter k-range of 3-10.5 $Å^{-1}$ was used for the three-shell fitting of data collected at 300 K. A fitting window of 1.5-3.5 Å was used for all fittings. To reduce the number of variables, all coordination numbers (CNs) were fixed based on the crystal structure of $Ag_{44}(SR)_{30}$. The energy shift of all fitting shells was correlated for each fit. For the four-shell fitting method, the Debye-Waller factors of two Ag-S shells were correlated to further reduce the number of variables.

2.3 EXAFS Simulation and Wavelet Transformed EXAFS

The simulation of both Ag K-edge and S K-edge EXAFS spectrum at 90 K was performed using the FEFF8 program code.[30] For Ag K-edge simulations, different crystal structure models with selected Ag sites were used based on the separation of Ag-S shells. The simulation of S K-edge EXAFS included 44 Ag atoms and 30 S atoms as the structure model. The S atoms in the bridging (1 atom) and base (4 atoms) positions in the capping mount motifs are chemically distinct and were selected as target atoms. The WT-EXAFS were generated by using a Morlet wave transform.[31] The k-range of 3-12.3 $Å^{-1}$ and 3-12 $Å^{-1}$ were used for the S K-edge and Ag K-edge, respectively. The wavelet parameters for S K-edge were set as 2.5 for η and 1 for σ, and η=4 and σ=1 were used for the Ag K-edge in order to have high resolution in k space.

3. RESULTS AND DISCUSSION

Determination of fitting shells

The FT-EXAFS spectra of Ag K-edge for $Ag_{44}(SR)_{30}$ at two different temperatures are shown in Figure 1. The peak at around 2 Å is attributed to the Ag-S bonds. The peak appearing slightly below 3 Å corresponds to the Ag-Ag bonds. The peak intensity of FT-EXAFS spectrum is mainly affected by the size of NCs and the Debye-Waller factor. This factor accounts for the thermal and structural disorder in samples, and a large Debye-Waller factor corresponds to a reduced FT-EXAFS intensity.[32] In this study, the difference in peak intensity at the two different temperatures comes from the Debye-Waller factor. At the lower temperature, thermal fluctuations are suppressed, which can lead to a smaller Debye-Waller factor and therefore higher peak intensities in the FT-EXAFS spectrum.[33]

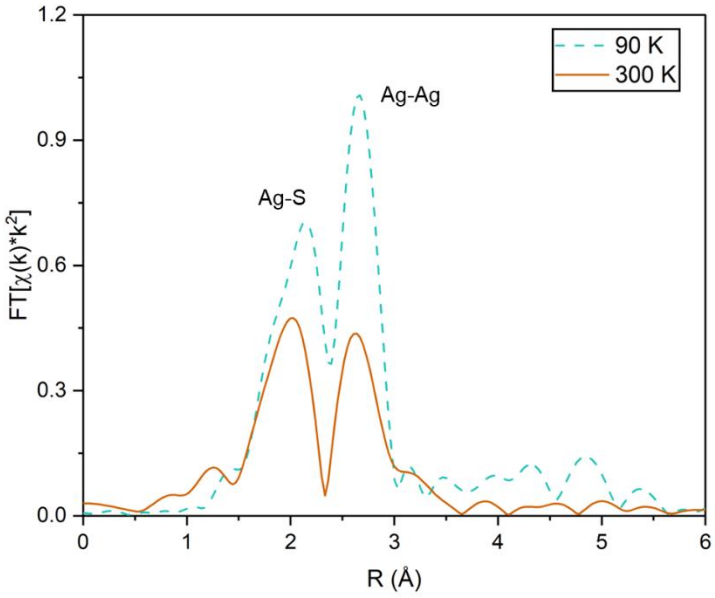

Figure 1. Ag K-edge FT-EXAFS spectra of $Ag_{44}(SR)_{30}$ at 90 K and 300 K.

In order to get detailed structural information from fitting the FT-EXAFS spectra of $Ag_{44}(SR)_{30}$, the site-specific bonding in the NCs was first analyzed.[18,20,26] using the structure that was experimentally measured by single-crystal X-ray diffraction.[6] As shown in Scheme 1, the

structure can be broken down into a hollow icosahedral Ag_{12} inner metal core, a dodecahedral Ag_{20} cage, and six $Ag_2(SR)_5$ mount motifs. It should be noticed that the 20 Ag atoms in the cage can be further distinguished into two chemically different sites due to the placement of the 6 capping mount motifs. Within the Ag_{20} structure, there are eight Ag atoms (light green atoms in Scheme 1) that can be considered as vertices of a cube, which are each bonded to three S atoms. The remaining 12 Ag atoms in the Ag_{20} structure can be grouped into six pairs, which are located above each face of the cube and are bonded to two S atoms. Thus, there are four different Ag coordination environments.

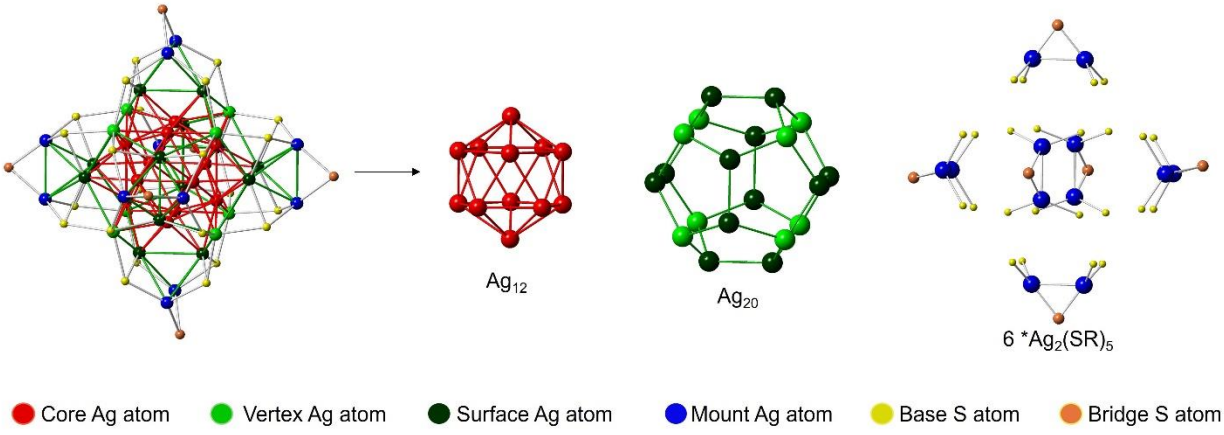

Scheme 1. The crystal structure of $Ag_{44}(SR)_{30}$ NCs with the indication of different Ag and S sites. The hydrocarbon portions of the thiolate ligands were omitted for clarity.

From inspection of the Ag-Ag bond length distribution (Figure 2), two distinct shells were identified. The first Ag-Ag shell (Ag-Ag1) consists of strong metallic bonds within the Ag_{12} core as well as bonds that link the Ag_{12} metal core to the Ag_{20} cage, which are consistent with the bulk Ag-Ag bond length. The second Ag-Ag shell (Ag-Ag2) are longer bonds that connect vertex, surface and mount Ag sites. The bonds at 3 Å could be a separate shell but the contribution of this shell to the overall FT-EXAFS is too small, which means it cannot be

resolved from the fitting. So, this shell was merged with those long bonds on the surface and considered as the second Ag-Ag shell.

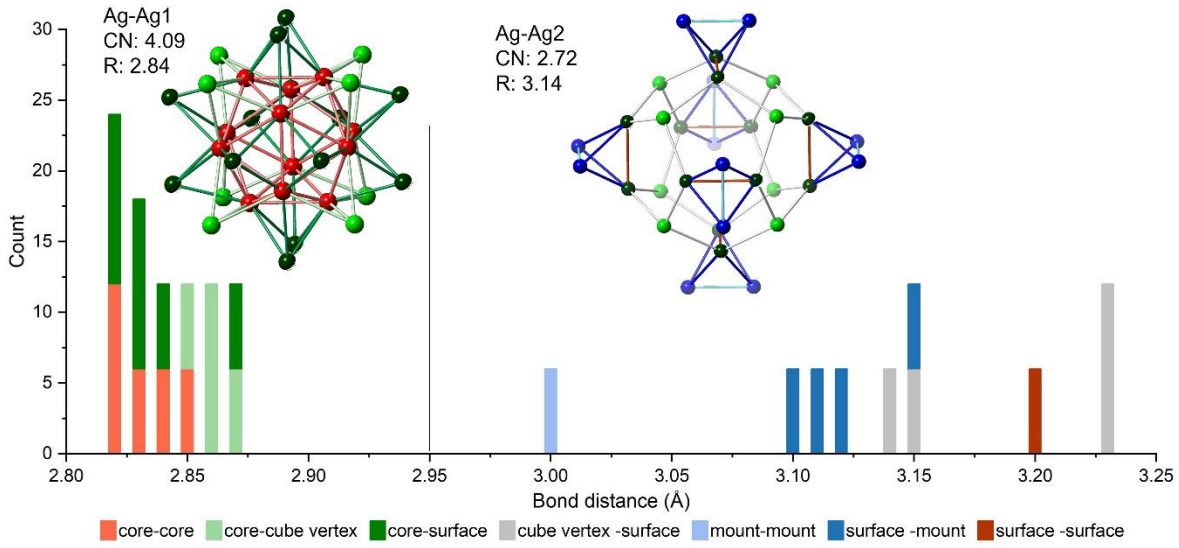

Figure 2. The bond length distribution of Ag-Ag bonds of $Ag_{44}(SR)_{30}$ with assigned FT-EXAFS fitting shells. The Ag-Ag1 bonds are those that connect the 12 Ag atoms in the icosahedral inner shell to one another as well as those that connect each Ag atom to the 20 faces of the icosahedron. The Ag-Ag2 bonds are those that connect the 20 Ag atoms in the decahedral outer shell to one another as well as those that connect six pairs of Ag atoms that straddle pairs of Ag atoms in the decahedron.

Since the $Ag_{44}(SR)_{30}$ NCs have 3D mount motifs, the S atoms could also experience different coordination environments, therefore it is worthwhile examining the Ag-S bond length distribution. As displayed in Figure 3, there are two Ag-S shells. The first shell includes the bonds between the S atoms in the base of the mounts to the mount Ag and the surface. The second shell includes the bonds between the S atoms in the base of the mounts to the vertex Ag atoms. The S atoms bonded to two mount Ag atoms (bridging S) are different from the remaining S atoms (base S).

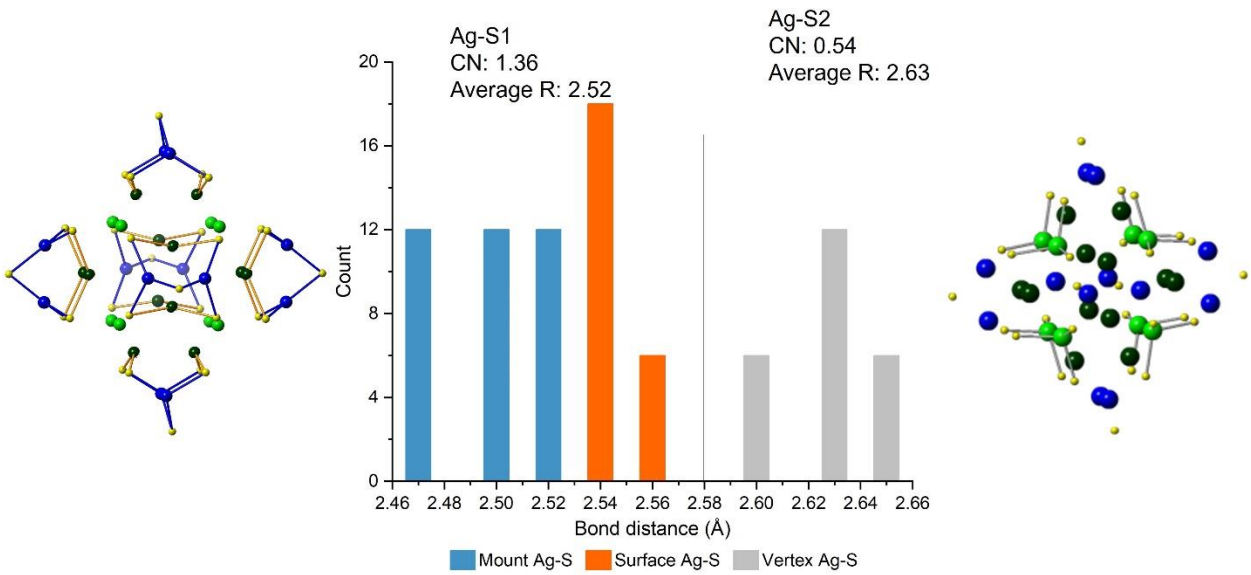

Figure 3. The bond length distribution of Ag-S bonds of $Ag_{44}(SR)_{30}$ with assigned FT-EXAFS fitting shells. (Yellow: S atom; blue: mount Ag atoms; dark green: surface Ag atoms; light green: vertex Ag atoms).

To verify if the two Ag-S shells are distinguishable in EXAFS, the Ag K-edge WT-EXAFS simulations were performed. As shown in Figure 4, the center of the strongest signal from the two shells appears at different k values. The first shell has the signal below ~4 $Å^{-1}$ in k space, and the major signal of the second shell appears above ~4 $Å^{-1}$. This shift could be due to the existence of two different Ag-S shells. However, there are two distinct areas appearing at high k region for Ag-S1 because of Ag-Ag interactions, which may contribute to the signal of Ag-S shell. To avoid the interference of Ag-Ag shells, the S K-edge WT-EXAFS simulation was further performed. It was found that the major signal areas have different shapes for the two different S sites (Figure 5). For the bridging S, there is only one area at around k ~4 $Å^{-1}$. This suggests that there is only one type of Ag-S bond between the mount S atoms and the mount Ag atoms, which is consistent with all mount Ag atoms being in chemically equivalent positions. For the base S atoms, however, the major signal area is at the same position, but it splits into two partially joined areas. This indicates that there are two types of bonds despite the fact that each

mount S atom is bonded to three chemically inequivalent Ag atoms: mount Ag, surface Ag, and vertex Ag. Although one may expect to observe three distinct types of bonds, the mount Ag-S and surface Ag-S bond lengths are close enough to merge into one Ag-S shell. The vertex Ag-S bonds are significantly longer, however, such that they represent a distinct Ag-S shell. Hence, only two distinct areas are observed for the mount S atom bonding, suggesting there are two Ag-S shells.

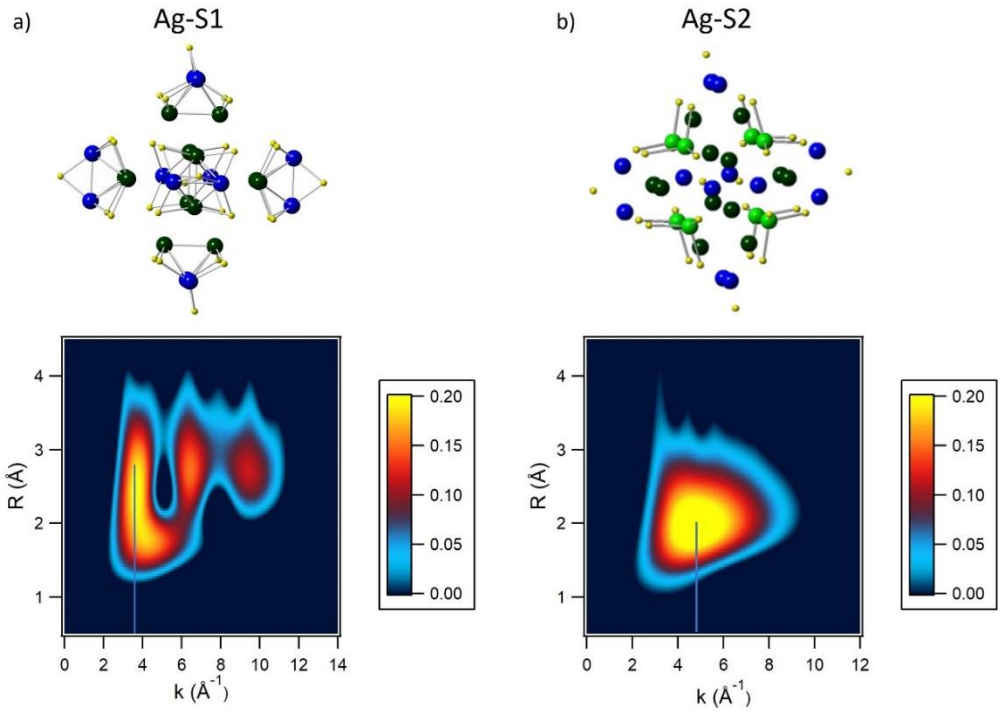

Figure 4. The WT-EXAFS simulations of Ag K-edge and the corresponding crystal structure for a) the Ag-S1 and b) the Ag-S2.

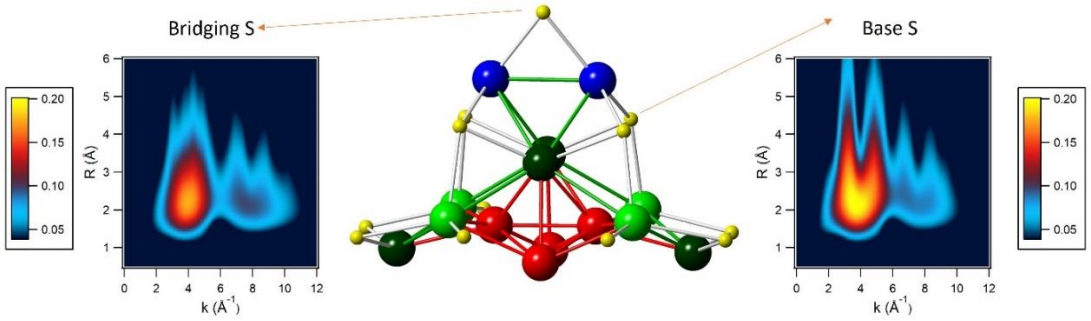

Figure 5. The WT-EXAFS simulations of S K-edge for the two distinct S sites.

Fitting method comparison

Based on the analysis of fitting shells, two Ag-S shells and two Ag-Ag shells were identified. The four-shell fitting method was therefore applied to the data collected at 90 K and 300 K, and the fitting results were compared with the traditional three-shell fitting method (one Ag-S shell and two Ag-Ag shells). Figure 6a and b show the fits by using four shells, which are similar to the fits obtained by using three shells (Figure S1). However, these two methods show obvious differences in Debye-Waller factors and R-factors, which are two parameters related to the fitting quality of EXAFS. The Debye-Waller factors can indicate the variation of bond length within a shell. If one shell contains bonds with a narrow range of length, the Debye-Waller factor will be small, and it can be considered to be a good fit. From the comparison of four-shell and three-shell fitting methods, the Debye-Waller factors of the Ag-S shell becomes smaller when two Ag-S shells were used (see Figure 6c), which means more suitable fitting shells are assigned to the FT peak. The R-factor is a statistical value to evaluate the differences between the fitting curve and experimental data. Typically, a good fit should have an R-factor less than 0.03. In this study, the R-factors can be reduced by applying a four-shell fitting method (

Table **1**). Particularly, the R-factor of 300 K data using the conventional three-shell method is 0.028, which is only slightly below 0.03. By applying the new four-shell method, the R-factor decreased significantly to 0.013. The decreases of Debye-Waller factors and R-factors further indicate the necessity of using two Ag-S shells. Moreover, the decreases of these two factors are more pronounced for data collected at 300 K than at a low temperature, which could be due to the different levels of noise. At a low temperature, thermal vibrations can be suppressed resulting in reduced noise level. Thus, the data collected at 300 K with high noise level is more sensitive to the fitting method. We can conclude that the determination of fitting shells is critical to get more reliable fitting results.

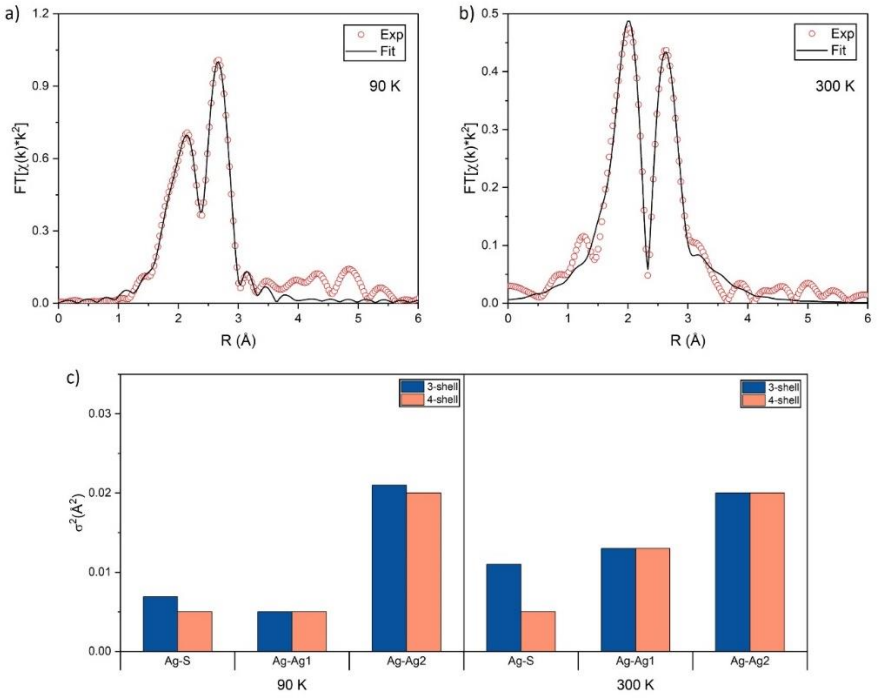

Figure 6. Ag K-edge FT-EXAFS spectrum of $Ag_{44}(SR)_{30}$ with four-shell fitting at a) 90 K and b) 300K. c) The comparison of Debye-Waller factors obtained by two fitting methods. The Debye-Waller factors for two Ag-S shells were correlated for four-shell fitting method, so they have the same value and only one bar was shown in the figure (Left panel: 90 K; right panel: 300K).

Insight into the Bonding Properties

The EXAFS fitting results of bonding distances from the two methods are plotted in Figure 7a-c. Comparing the trend observed from three-shell and four-shell fitting methods, the Ag-S shells show different results (Figure 7a). When only one Ag-S shell was applied, the Ag-S bonds showed no obvious change as the temperature increased from 90 K to 300 K. However, when two Ag-S shells were included, the bond distances of the Ag-S1 shell were unchanged while the bond distances of Ag-S2 shell increased when the temperature increased from 90 K to 300 K. From the crystal structure, the Ag-S1 shell consists of Ag-S bonds within the mount motifs. These Ag-S1 bonds are more closely related to the thiolate ligands than the Ag-S2 bonds. The thiolate ligands have a preferred orientation due to the existence of π-π interactions between the ligands. Hence, the Ag-S1 shell can be considered as a rigid ligand shell (blue bonds in Figure 7d) and does not sensitively respond to the temperature change. The Ag-S2 shell (red bonds in Figure 7d) represents the linkage between mount motifs and the Ag_{32} core structure, which appears to be more flexible compared with the Ag-S1 bonds within mount motifs, because the π-π interactions are weak between different motifs as shown in Figure S2. The notion of the rigid ligand shell separated from the Ag_{32} metal core observed in this work is interesting as the similar concept of rigid rings was observed in thiolate protected Au NCs.[34–36] In addition, the distinct nature of each type of Ag-S bonds can result in different bonding behavior. The metallic nature of the Ag sites decreases when moving outward, away from the Ag_{12} metal core, which can affect Ag-S bonding. In particular, the vertex Ag atoms have more metallic characteristics than the surface and mount Ag atoms such that when they are bonded with S atoms, the Ag-S2 bonds can exhibit normal expansion behavior. The increase of the Ag-S2 shell bond distances at a higher temperature cannot be observed in the one Ag-S shell fitting results because the contribution of the Ag-S2 shell to the overall Ag-S shell is small, which only accounts for about

28% of all Ag-S bonds (Figure S3). Since XAS is an averaging technique, the bond length change of whole Ag-S shell is dominated by the change of the first Ag-S shell. Thus, the improved fitting method allows us to distinguish the unique bonding behavior of different Ag-S motifs from a site-specific perspective.

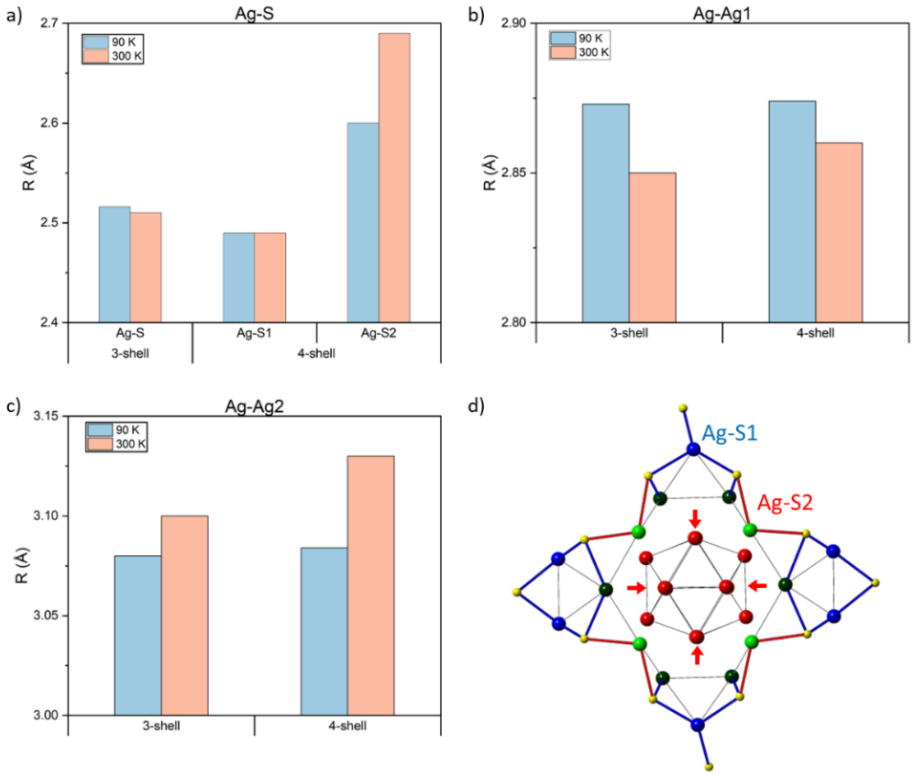

Figure 7. The comparison of bond distances at different temperatures by using 3-shell and 4-shell fitting methods for a) Ag-S shell, b) Ag-Ag1 shell and c) Ag-Ag2 shell. d) Schematic illustration of two Ag-S shells, and the indication of metal core bond distance changes upon temperature increase.

On the other hand, the Ag-Ag shells show similar trends between these two methods, although their magnitudes differ. The Ag-Ag1 shell shows bond contraction, and the Ag-Ag2 shell shows bond expansion as the temperature increases (Figure 7b-d). The negative thermal expansion exhibited by the metal core is not commonly observed in thiolate protected NCs. For $Au_{25}(SR)_{18}$, its structure contains of an icosahedral Au_{13} metal core, which experiences a bond expansion

with the increase of temperature.[20] Previously, the negative thermal behavior was observed for Au NCs with face-centered cubic (FCC)-like metal core because of the existence of Au_4 tetrahedral units.[22,26] For thiolate protected Ag NCs, the negative thermal behavior was observed in Ag_{13} metal core for Ag_{25} NCs, but the major structure units corresponds to this uncommon behavior are also 4-atom tetrahedral units.[21] In this study, the unique bonding behavior of metal core for $Ag_{44}(SR)_{30}$ is particularly interesting due to the absence of the central atom of the metal core. The hollow icosahedral Ag_{12} metal core could result in significant molecule-like behavior like those NCs with tetrahedral structure units in the metal core.[16,26] Such a hollow metal core structure is rarely observed in thiolate protected NCs. The Au_{144} NCs is one of the atomically precise NCs that have a hollow icosahedral Au_{12} inner shell within the metal core,[37] though the absence of central atom would not have large impact on the overall bonding properties of NCs due to their large size. However, for small NCs like $Ag_{44}(SR)_{30}$, the contribution of each atom could have a large impact on the overall bonding properties. Our results imply that only one atom missing in such small NCs could significantly change the bonding behavior of the metal core.

Table 1. EXAFS three-shell (top) and four-shell (bottom) fitting results for $Ag_{44}(SR)_{30}$ NCs at 90 K and 300 K

Temperature (K)	**Shell**	**CN (Fixed)**	**R (Å)**	**σ^2 (Å^2)**	**ΔE_0 (eV)**	**R factor**
90	Ag-S	1.9	2.516 (5)	0.0069 (6)	3.5 (4)	0.0015
	Ag-Ag1	4.09	2.873 (2)	0.0050 (2)		
	Ag-Ag2	2.72	3.08 (2)	0.021 (4)		
300	Ag-S	1.9	2.51 (2)	0.011 (2)	3 (2)	0.028
	Ag-Ag1	4.09	2.85 (2)	0.013 (2)		

	Ag-Ag2	2.72	3.10 (7)	0.02 (2)		
90	Ag-S1	1.36	2.490 (8)	0.005 (2)	3.6 (5)	0.0013
	Ag-S2	0.54	2.60 (4)			
	Ag-Ag1	4.09	2.874 (3)	0.0050 (2)		
	Ag-Ag2	2.72	3.084 (4)	0.020 (4)		
300	Ag-S1	1.36	2.49 (2)	0.005 (1)	4 (2)	0.013
	Ag-S2	0.54	2.69 (4)			
	Ag-Ag1	4.09	2.86 (2)	0.013 (1)		
	Ag-Ag2	2.72	3.13 (5)	0.02 (1)		

4. CONCLUSIONS

In conclusion, the bonding properties of $Ag_{44}(SR)_{30}$ have been examined with EXAFS from a site-specific perspective. The WT-EXAFS simulations were helpful for the determination of fitting shells. It was found that there are two Ag-S shells and two Ag-Ag shells in $Ag_{44}(SR)_{30}$. The four-shell fitting method was applied to the data collected at 90 K and 300 K. This new structure analysis method shows increased EXAFS fitting quality as evidenced by improved R-factor and Debye-Waller factors. Given the improvement of the fitting for $Ag_{44}(SR)_{30}$ at both temperatures, the close comparison of bond distance change due to temperature effect is more reliable. It shows that the vertex Ag-S2 bonds exhibit a considerable increase of bond distance, which is different from surface and mount Ag-S1 bonds. This observation of different bonding properties within the Ag-S motifs cannot be achieved without using two Ag-S shells in the analysis of EXAFS. The metal core of $Ag_{44}(SR)_{30}$ shows negative thermal expansion and molecule-like behavior, which is not common to NCs and could be attributed to the absence of a center atom in the icosahedral core. It also suggests a possible structure-function relationship that could guide the development of new NC materials such as removing one atom or doping with

different atoms. The new EXAFS fitting method developed in this work can be extended to the analysis of other NCs, especially of NC's with different mount formation, such as the monomer and trimer mount motifs.[38] The insights developed from the exploration of different NCs can provide more reliable structure details for comparison and modeling prediction, and also a more site-specific analysis especially for the metal-ligand shell. The new temperature-dependent bonding properties uncovered in this work could provide deeper comprehension into the structure-property relationship, which can also help with the design of new NC materials with desired properties such as enhance stability for industrial applications.

ASSOCIATED CONTENT

Supporting Information.

The following files are available free of charge.

Supporting figures of Ag K-edge FT-EXAFS spectrum of $Ag_{44}(SR)_{30}$ with three-shell fitting at 90 K and 300K and bond length distribution of Ag-S bonds (PDF)

AUTHOR INFORMATION

Corresponding Authors

Peng Zhang − Department of Chemistry, Dalhousie University, Halifax, NS B3H 4R2, Canada; E-mail: peng.zhang@dal.ca

Authors

Ziyi Chen − Department of Chemistry, Dalhousie University, Halifax, NS B3H 4R2, Canada

Daniel M. Chevrier − Aix-Marseille University, French Alternative Energies and Atomic Energy Commission (CEA), French National Center for Scientific Research (CNRS), UMR7265

Institute of Biosciences and Biotechnologies of Aix-Marseille (BIAM), Saint-Paul-lez-Durance, 13108 France

Brian E. Conn – Adhesive Technologies and Functional Coatings, Henkel Corporation, Madison Heights, MI 48071, United States

Terry P. Bigioni – Department of Chemistry and Biochemistry, University of Toledo, Toledo, Ohio 43606, United States

Notes

The authors declare no competing financial interests.

ACKNOWLEDGMENTS

The authors would like to thank the financial support from NSERC Canada. This research used resources of the Advanced Photon Source, an Office of Science User Facility operated for the US Department of Energy (DOE) Office of Science by Argonne National Laboratory, and was supported by the US DOE under contract no. DE-AC02-06CH11357, and the Canadian Light Source (CLS) and its funding partners. The CLS is supported by the CFI, NSERC, NRC, CIHR, the University of Saskatchewan, the Government of Saskatchewan, and Western Economic Diversification Canada. Z.C. would like to acknowledge the PhD Entrance scholarship from Dalhousie University and the Nova Scotia Graduate Scholarship – Doctoral. T.P.B. thanks the National Science Foundation for financial support (Grant No 1905262).

REFERENCES

(1) Du, Y.; Sheng, H.; Astruc, D.; Zhu, M. Atomically Precise Noble Metal Nanoclusters as Efficient Catalysts: A Bridge between Structure and Properties. *Chem. Rev.* **2020**, *120*, 526–622. DOI: 10.1021/acs.chemrev.8b00726.

(2) Kang, X.; Li, Y.; Zhu, M.; Jin, R. Atomically Precise Alloy Nanoclusters: Syntheses, Structures, and Properties. *Chem. Soc. Rev.* **2020**, *49*, 6443–6514. DOI: 10.1039/C9CS00633H.

(3) Walsh, A. G.; Zhang, P. Thiolate-Protected Bimetallic Nanoclusters: Understanding the Relationship between Electronic and Catalytic Properties. *J. Phys. Chem. Lett.* **2021**, *12*, 257–275. DOI: 10.1021/acs.jpclett.0c03252.
(4) Walsh, A. G.; Zhang, P. Thiolate-Protected Single-Atom Alloy Nanoclusters: Correlation between Electronic Properties and Catalytic Activities. *Adv. Mater. Interfaces* **2021**, *8*, 2001342. DOI: 10.1002/admi.202001342.
(5) Joshi, C. P.; Bootharaju, M. S.; Alhilaly, M. J.; Bakr, O. M. $[Ag_{25}(SR)_{18}]^-$: The "Golden" Silver Nanoparticle. *J. Am. Chem. Soc.* **2015**, *137*, 11578–11581. DOI: 10.1021/jacs.5b07088.
(6) Desireddy, A.; Conn, B. E.; Guo, J.; Yoon, B.; Barnett, R. N.; Monahan, B. M.; Kirschbaum, K.; Griffith, W. P.; Whetten, R. L.; Landman, U.; et al. Ultrastable Silver Nanoparticles. *Nature* **2013**, *501*, 399–402. DOI: 10.1038/nature12523.
(7) Qian, H.; Eckenhoff, W. T.; Zhu, Y.; Pintauer, T.; Jin, R. Total Structure Determination of Thiolate-Protected Au_{38} Nanoparticles. *J. Am. Chem. Soc.* **2010**, *132*, 8280–8281. DOI: 10.1021/ja103592z.
(8) Yang, H.; Wang, Y.; Huang, H.; Gell, L.; Lehtovaara, L.; Malola, S.; Häkkinen, H.; Zheng, N. All-Thiol-Stabilized Ag_{44} and $Au_{12}Ag_{32}$ Nanoparticles with Single-Crystal Structures. *Nat. Commun.* **2013**, *4*, 2422. DOI: 10.1038/ncomms3422.
(9) Wan, X.-K.; Wang, J.-Q.; Wang, Q.-M. Ligand-Protected Au_{55} with a Novel Structure and Remarkable CO_2 Electroreduction Performance. *Angew. Chem. Int. Ed.* **2021**, *60*, 20748–20753. DOI: 10.1002/anie.202108207.
(10) Higaki, T.; Li, Y.; Zhao, S.; Li, Q.; Li, S.; Du, X.-S.; Yang, S.; Chai, J.; Jin, R. Atomically Tailored Gold Nanoclusters for Catalytic Application. *Angew. Chem.* **2019**, *131*, 8377–8388. DOI: 10.1002/ange.201814156.
(11) Xie, Y.-P.; Shen, Y.-L.; Duan, G.-X.; Han, J.; Zhang, L.-P.; Lu, X. Silver Nanoclusters: Synthesis, Structures and Photoluminescence. *Mater. Chem. Front.* **2020**, *4*, 2205–2222. DOI: 10.1039/D0QM00117A.
(12) Cowan, M. J.; Mpourmpakis, G. Structure–Property Relationships on Thiolate-Protected Gold Nanoclusters. *Nanoscale Adv.* **2019**, *1*, 184–188. DOI: 10.1039/C8NA00246K.
(13) Zhang, P. X-Ray Spectroscopy of Gold–Thiolate Nanoclusters. *J. Phys. Chem. C* **2014**, *118*, 25291–25299. DOI: 10.1021/jp507739u.
(14) Chen, Z.; Walsh, A. G.; Wei, X.; Zhu, M.; Zhang, P. Site-Specific Electronic Properties of $[Ag_{25}(SR)_{18}]^-$ Nanoclusters by X-Ray Spectroscopy. *Small* **2021**, *17*, 2005162. DOI: 10.1002/smll.202005162.
(15) Christensen, S. L.; MacDonald, M. A.; Chatt, A.; Zhang, P.; Qian, H.; Jin, R. Dopant Location, Local Structure, and Electronic Properties of $Au_{24}Pt(SR)_{18}$ Nanoclusters. *J. Phys. Chem. C* **2012**, *116*, 26932–26937. DOI: 10.1021/jp310183x.
(16) Chevrier, D. M.; Zeng, C.; Jin, R.; Chatt, A.; Zhang, P. Role of Au_4 Units on the Electronic and Bonding Properties of $Au_{28}(SR)_{20}$ Nanoclusters from X-Ray Spectroscopy. *J. Phys. Chem. C* **2015**, *119*, 1217–1223. DOI: 10.1021/jp509296w.
(17) Chevrier, D. M.; MacDonald, M. A.; Chatt, A.; Zhang, P.; Wu, Z.; Jin, R. Sensitivity of Structural and Electronic Properties of Gold–Thiolate Nanoclusters to the Atomic Composition: A Comparative X-Ray Study of $Au_{19}(SR)_{13}$ and $Au_{25}(SR)_{18}$. *J. Phys. Chem. C* **2012**, *116*, 25137–25142. DOI: 10.1021/jp309283y.
(18) Chevrier, D. M.; Conn, B. E.; Li, B.; Jiang, D.; Bigioni, T. P.; Chatt, A.; Zhang, P. Interactions between Ultrastable $Na_4Ag_{44}(SR)_{30}$ Nanoclusters and Coordinating Solvents:

Uncovering the Atomic-Scale Mechanism. *ACS Nano* **2020**, *14*, 8433–8441. DOI: 10.1021/acsnano.0c02615.
(19) MacDonald, M. A.; Zhang, P.; Chen, N.; Qian, H.; Jin, R. Solution-Phase Structure and Bonding of $Au_{38}(SR)_{24}$ Nanoclusters from X-Ray Absorption Spectroscopy. *J. Phys. Chem. C* **2011**, *115*, 65–69. DOI: 10.1021/jp1102884.
(20) MacDonald, M. A.; Chevrier, D. M.; Zhang, P.; Qian, H.; Jin, R. The Structure and Bonding of $Au_{25}(SR)_{18}$ Nanoclusters from EXAFS: The Interplay of Metallic and Molecular Behavior. *J. Phys. Chem. C* **2011**, *115*, 15282–15287. DOI: 10.1021/jp204922m.
(21) Chen, Z.; Walsh, A. G.; Wei, X.; Zhu, M.; Zhang, P. New Insights into the Bonding Properties of $[Ag_{25}(SR)_{18}]^-$ Nanoclusters from X-Ray Absorption Spectroscopy. *J. Phys. Chem. C* **2022**, *126*, 12721–12727. DOI: 10.1021/acs.jpcc.2c04482.
(22) Yang, R.; Chevrier, D. M.; Zeng, C.; Jin, R.; Zhang, P. Bonding Properties of FCC-like $Au_{44}(SR)_{28}$ Clusters from X-Ray Absorption Spectroscopy. *Can. J. Chem.* **2017**, *95*, 1220–1224. DOI: 10.1139/cjc-2017-0169.
(23) Funke, H.; Chukalina, M.; Scheinost, A. C. A New FEFF-Based Wavelet for EXAFS Data Analysis. *J. Synchrotron Radiat.* **2007**, *14*, 426–432. DOI: 10.1107/S0909049507031901.
(24) Penfold, T. J.; Tavernelli, I.; Milne, C. J.; Reinhard, M.; Nahhas, A. E.; Abela, R.; Rothlisberger, U.; Chergui, M. A Wavelet Analysis for the X-Ray Absorption Spectra of Molecules. *J. Chem. Phys.* **2013**, *138*, 014104. DOI: 10.1063/1.4772766.
(25) Martini, A.; Signorile, M.; Negri, C.; Kvande, K.; Lomachenko, K. A.; Svelle, S.; Beato, P.; Berlier, G.; Borfecchia, E.; Bordiga, S. EXAFS Wavelet Transform Analysis of Cu-MOR Zeolites for the Direct Methane to Methanol Conversion. *Phys. Chem. Chem. Phys.* **2020**, *22*, 18950–18963. DOI: 10.1039/D0CP01257B.
(26) Chevrier, D. M.; Chatt, A.; Zhang, P.; Zeng, C.; Jin, R. Unique Bonding Properties of the $Au_{36}(SR)_{24}$ Nanocluster with FCC-Like Core. *J. Phys. Chem. Lett.* **2013**, *4*, 3186–3191. DOI: 10.1021/jz401818c.
(27) Yang, R.; Morris, D. J.; Higaki, T.; Ward, M. J.; Jin, R.; Zhang, P. New Insights on the Bonding Properties of BCC-like $Au_{38}S_2(SR)_{20}$ Nanoclusters from X-Ray Absorption Spectroscopy. *J. Phys. Chem. C* **2018**, *122*, 22776–22782. DOI: 10.1021/acs.jpcc.8b07551.
(28) Conn, B. E.; Desireddy, A.; Atnagulov, A.; Wickramasinghe, S.; Bhattarai, B.; Yoon, B.; Barnett, R. N.; Abdollahian, Y.; Kim, Y. W.; Griffith, W. P.; et al. M_4Ag_{44}(p-MBA)$_{30}$ Molecular Nanoparticles. *J. Phys. Chem. C* **2015**, *119*, 11238–11249. DOI: 10.1021/jp512237b.
(29) Ravel, B.; Newville, M. ATHENA, ARTEMIS, HEPHAESTUS: Data Analysis for X-Ray Absorption Spectroscopy Using IFEFFIT. *J. Synchrotron Radiat.* **2005**, *12*, 537–541. DOI: 10.1107/S0909049505012719.
(30) Ankudinov, A. L.; Ravel, B.; Rehr, J. J.; Conradson, S. D. Real-Space Multiple-Scattering Calculation and Interpretation of X-Ray Absorption near-Edge Structure. *Phys. Rev. B* **1998**, *58*, 7565–7576. DOI: 10.1103/PhysRevB.58.7565.
(31) Funke, H.; Scheinost, A. C.; Chukalina, M. Wavelet Analysis of Extended X-Ray Absorption Fine Structure Data. *Phys. Rev. B* **2005**, *71*, 094110. DOI: 10.1103/PhysRevB.71.094110.

(32) Dimakis, N.; Bunker, G. *Ab Initio* Single- and Multiple-Scattering EXAFS Debye-Waller Factors: Raman and Infrared Data. *Phys. Rev. B* **1998**, *58*, 2467–2475. DOI: 10.1103/PhysRevB.58.2467.
(33) Guliamov, O.; Frenkel, A. I.; Menard, L. D.; Nuzzo, R. G.; Kronik, L. Tangential Ligand-Induced Strain in Icosahedral Au_{13}. *J. Am. Chem. Soc.* **2007**, *129*, 10978–10979. DOI: 10.1021/ja0725706.
(34) Han, W.; Liu, P.; Zheng, M.; Zeng, X. C.; Xu, W. W. Ring Model for Understanding How Interfacial Interaction Dictates the Structures of Protection Motifs and Gold Cores in Thiolate-Protected Gold Nanoclusters. *J. Phys. Chem. Lett.* **2021**, *12*, 3006–3013. DOI: 10.1021/acs.jpclett.1c00544.
(35) Natarajan, G.; Mathew, A.; Negishi, Y.; Whetten, R. L.; Pradeep, T. A Unified Framework for Understanding the Structure and Modifications of Atomically Precise Monolayer Protected Gold Clusters. *J. Phys. Chem. C* **2015**, *119*, 27768–27785. DOI: 10.1021/acs.jpcc.5b08193.
(36) Yamazoe, S.; Takano, S.; Kurashige, W.; Yokoyama, T.; Nitta, K.; Negishi, Y.; Tsukuda, T. Hierarchy of Bond Stiffnesses within Icosahedral-Based Gold Clusters Protected by Thiolates. *Nat. Commun.* **2016**, *7*, 10414. DOI: 10.1038/ncomms10414.
(37) Yan, N.; Xia, N.; Liao, L.; Zhu, M.; Jin, F.; Jin, R.; Wu, Z. Unraveling the Long-Pursued Au144 Structure by X-Ray Crystallography. *Sci. Adv.* **2018**, *4*, eaat7259. DOI: 10.1126/sciadv.aat7259.
(38) Conn, B. E.; Atnagulov, A.; Yoon, B.; Barnett, R. N.; Landman, U.; Bigioni, T. P. Confirmation of a de Novo Structure Prediction for an Atomically Precise Monolayer-Coated Silver Nanoparticle. *Sci. Adv.* **2016**, *2*, e1601609. DOI: 10.1126/sciadv.1601609.

TOC GRAPHICS